

# True Muonium ( $\mu^+\mu^-$ ) on the Light Front

Henry Lamm\* and Richard F. Lebed†

Department of Physics, Arizona State University, Tempe, AZ 85287

(Dated: April, 2014)

Applying Discretized Light Cone Quantization, we perform the first calculation of the spectrum of true muonium, the  $\mu^+\mu^-$  atom, as modified by the inclusion of an  $|e\bar{e}\rangle$  Fock component. The shift in the mass eigenvalue is found to be largest for triplet states. If  $m_e$  is taken to be a substantial fraction of  $m_\mu$ , the integrated probability of the electronic component of the  $1^3S_1$  state is found to be as large as  $O(10^{-2})$ . Initial studies of the Lamb shift for the atom are performed. Directions for making the simulations fully realistic are discussed.

PACS numbers: 36.10.Ee, 11.10.Ef, 11.10.St, 12.20.Ds

## I. INTRODUCTION

The atom consisting of a  $\mu^+\mu^-$  bound state, called *true muonium* [in distinction from conventional muonium, the atom  $(\mu^+e^-)$ ] has not yet been identified, despite much more exotic bound states having been successfully characterized, such as  $\pi\mu$  atoms [1] and even the dipositronium  $(e^+e^-)(e^+e^-)$  molecule [2]. While  $(\mu^+\mu^-)$  atoms have doubtless been produced many times, for example in  $e^+e^-$  colliders (where they can be easily lost in the beam line before decaying), it is only recently that immediately realizable experiments have been proposed to generate sufficient numbers of true muonium atoms to guarantee their unambiguous observation. Ideas include  $e^+e^-$  collider experiments in which the beams intersect at an angle rather than head on [thus projecting  $(\mu^+\mu^-)$  along the beam bisector] or conventional setups in which the produced  $(\mu^+\mu^-)$  recoils against a co-produced photon [3], or producing  $(\mu^+\mu^-)$  as a byproduct of experiments that scatter electron beams from high- $Z$  fixed targets in search of hidden-sector *heavy photons* [4].

True muonium consists of a spectrum of metastable states (lifetimes in the ps to ns range [3]), for which the 2.2  $\mu$ s muon weak decay lifetime is effectively infinite. The transitions are therefore overwhelmingly electromagnetic, meaning that  $(\mu^+\mu^-)$  can be treated, like positronium  $(e^+e^-)$ , as a Bohr atom [in the  $(\mu^+\mu^-)$  case, with a ground-state radius of only 512 fm], and its transitions can be computed using QED. Unlike positronium, its decay products include not only monochromatic photons, but also  $e^+e^-$  pairs of well-characterized energies. Studies of  $(\mu^+\mu^-)$  are further motivated by discrepancies in precision muon-related effects, such as  $(g-2)_\mu$  and the proton charge radius [5, 6].

As far as an isolated  $(\mu^+\mu^-)$  bound state is concerned, conventional QED and quantum-mechanical wave functions are generally sufficient to compute its most important features, just as is true for  $(e^+e^-)$ . However, these techniques provide not as much guidance for understanding the detailed structure-dependent dynamics

of the atoms. Indeed, remarkable experiments can in principle be performed on these “atoms in flight”, including measurements of the Lamb shift [7]. Bound states in quantum field theory (QFT) are notoriously complicated objects, due not only to the fact that the vacuum consists of an arbitrarily large number of virtual particles, but also because the constituents can be relativistic, and the required boosts to relate the components of the wave function depend in a detailed way upon the interaction.

In fact, a well-known method of studying bound states avoids these problems. By performing quantization not, as usual, with respect to conventional time  $t$  (called *instant form*) but rather with respect to the light-front time  $x^+ \equiv t + z$  (called *front form*) [8], one develops a Hamiltonian formalism that is nonetheless fully covariant and ideally suited to characterizing bound states comprised of well-defined constituents [9]. The analogue to a Schrödinger equation for the state then becomes an infinite but denumerable set of coupled integral equations. In order to obtain numerical results, one may then truncate the equations by limiting the set of component Fock states included in the calculation and discretizing momenta with suitable periodic boundary conditions, effectively turning infinite-dimensional matrices into finite ones and creating a problem solvable on a computer, which is termed Discretized Light-Cone Quantization (DLCQ) [10].

Our purpose in this article is to report on the first simulation of the true muonium atom using DLCQ and other light-front techniques. We borrow heavily on older works that use this approach to simulate positronium. The first such attempt [11] was impeded by slow numerical convergence, which was successfully addressed by a better treatment [12] of the singularity induced by the Coulomb interaction. Further work [13] superseded the effective interaction approach of [12] to perform a direct diagonalization of the Hamiltonian matrix. The work of Trittmann and Pauli [14] unified these improvements, and additionally included in the Fock space the explicit single-photon annihilation channel  $|\gamma\rangle$ . They also demonstrated the numerical restoration of rotational invariance, a needed improvement since light-front coordinates treat the longitudinal and transverse directions very differently. Our work is a direct application of the methods introduced

\* hllammiv@asu.edu

† Richard.Lebed@asu.edu

in Ref. [14] to true muonium; our principal innovation, apart from the trivial substitution of the valence electrons with muons, is the inclusion of  $|e\bar{e}\rangle$  Fock states, which can mix with the  $|\mu\bar{\mu}\rangle$  component via the explicit  $|\gamma\rangle$  component. We also apply a subtraction to the interaction amplitudes in order to regularize the ultraviolet behavior of observables.

The positronium simulations of Ref. [14] adopted the unphysically large value  $\alpha = 0.3$  in order to show the robustness of the method at large values of coupling, where high-order QED calculations begin to become unreliable. An additional purpose for this choice was to provide numerical evidence that strong-coupling DLCQ would be applicable to the much more intricate QCD bound-state problem. In our calculations presented here, we maintain this large value of  $\alpha$  in order to study the effects of a large  $|e\bar{e}\rangle$  component of true muonium; of course,  $\alpha$  is an adjustable parameter of the program and can be altered for more physical simulations in our future work. Moreover, the code designed by Ref. [14] contains only one fermion mass parameter,  $m_e$  in their case and  $m_\mu$  in ours. In the present work,  $m_e$  is an independent parameter; again, to study the effects of a large  $|e\bar{e}\rangle$  component, we allow  $m_e$  to be any finite fraction of  $m_\mu$ . Ultimately, for physical applications one sets  $m_e/m_\mu \simeq 4.8 \cdot 10^{-3}$ , but we exhibit results with  $m_e/m_\mu = O(1)$  for the practical reason that properly characterizing a system in QFT with two widely separated scales requires proper renormalization evolution between the scales (In front form, the original diagrammatic renormalization techniques are described in Ref. [15]). Since the evolution typically depends upon the log of the ratio of scales, choosing  $m_e$  not excessively small compared to  $m_\mu$  minimizes this effect; we plan to address this important issue thoroughly in a subsequent paper [16].

Even with a large  $|e\bar{e}\rangle$  component, our simulations reproduce the Bohr spectrum of true muonium to a high degree of precision. Nevertheless, the significance of the  $|e\bar{e}\rangle$  component is clearly seen in the true muonium eigenvalues, and especially in the wave functions. We also see modifications to the  $(\mu^+\mu^-)$  Lamb shift in agreement with its expected dependence upon the atom's principal quantum number  $n$ . While the proper numerical and formal treatment of the  $|e\bar{e}\rangle$  sector will require future improvements (the effects of neglecting which are exhibited and discussed in detail below), we find these initial results to be very encouraging.

This paper is organized as follows. In Sec. II, we present essential conceptual and formal details of light-front bound-state techniques relevant to this work, and describe the associated numerical details in Sec. III. We define our model in Sec. IV and discuss the effects of the  $|e\bar{e}\rangle$  component in Sec. V. Section VI provides a discussion of the effect of momentum-space cutoffs, lepton mass renormalization, and the regularization of interaction amplitudes. We present our results in Sec. VII, with conclusions in Sec. VIII and details of the calculation of the relevant matrix elements in the Appendix.

## II. LIGHT-FRONT BOUND STATES

The action-functional approach has become the predominant method for performing QFT calculations. It is based upon a Lorentz-invariant Lagrangian density, and the symmetries of the theory (including gauge invariance) can be incorporated very efficiently. On the other hand, the Hamiltonian formalism provides a more natural language for describing bound-state systems, just as it does in non-relativistic quantum mechanics. However, Hamiltonians are complicated objects in relativistic QFT, especially in the instant form: The nonanalytic nature of the operator  $\sqrt{\mathbf{P}^2 + M^2}$  causes difficulties; the constituent particles have distinct rest frames, and the boost operations necessary to express them as part of a single wave function depend intrinsically upon the interactions between them; and most significantly, the vacuum structure is exceedingly complicated due to the creation and annihilation of virtual states with arbitrarily large numbers of quanta.

The front form addresses each of these difficulties. First, the Hamiltonian operator  $P^- \equiv P^0 - P^3$  conjugate to the time coordinate  $x^+$  is related linearly to the energy-squared operator,

$$H_{\text{LC}} = P^- P^+ - \mathbf{P}_\perp^2, \quad (1)$$

where  $P^+ \equiv P^0 + P^3$  is the longitudinal momentum component conjugate to the light-front longitudinal direction  $x^- \equiv t - z$ , and the transverse momentum is  $\mathbf{P}_\perp \equiv P^1 \mathbf{x} + P^2 \mathbf{y}$ . For an eigenvalue  $M^2$  of the operator  $H_{\text{LC}}$  corresponding to a state  $|\Psi\rangle$ , the light-front Hamiltonian eigenvalue equation is no longer nonanalytic:

$$P^- |\Psi\rangle = \frac{M^2 + \mathbf{P}_\perp^2}{P^+} |\Psi\rangle. \quad (2)$$

Second, out of the 10 Poincaré generators  $P^\mu$  and  $M^{\mu\nu}$ , the front form is special in having 7 that leave the time slice  $x^+ = \text{const}$  invariant [8], and therefore can be expressed without reference to the specific interaction in the Hamiltonian. These so-called *kinematic* operators are the spatial momentum components  $\mathbf{P}_\perp$ ,  $P^+$ , the longitudinal angular momentum ( $M^{12} = J_z$ ) and boost ( $M^{+-} = K_z$ ) generators, and the mixed transverse-longitudinal boosts  $M^{+\perp}$ . In contrast, the instant form has only 6 kinematic operators: the spatial momentum  $P^i$  and angular momentum  $M^{ij}$  components; in particular, the boost generators  $M^{0i}$  are all *dynamic*, in that they depend upon the interaction. Although the front form addresses the boost issue by providing kinematic boost generators, the price is the loss of manifest rotational invariance (the absence of simple  $\mathbf{J}_\perp$  generators), which is apparent from the fact that front form treats  $x^3$  differently from  $x^{1,2}$ . The  $P^\mu$  and total spin operators  $S^2$  and  $S_z$  still commute in front form, meaning that a particular state  $|\Psi\rangle$  can be completely specified as

$$|\Psi; M, P^+, \mathbf{P}_\perp, S^2, S_z; h\rangle, \quad (3)$$

where  $h$  indicates any discrete or non-spacetime quantum numbers, such as parity or lepton number.

Third, and most significantly, the numerical values of longitudinal momenta  $P^+$  for all physical particles are nonnegative, since  $P^0 = E > P^3$ . One cannot create virtual particles traveling “backwards” with respect to the light-front longitudinal direction, so empty space cannot produce collections of virtual particles in front form, in stark contrast to the situation in instant form. The ground state of the free theory is also the ground state of the full interacting theory, and the Fock state expansion built upon the free vacuum provides a rigorous “parton” component description of the full interacting state.

To be specific, the state  $|\Psi\rangle$  may be expressed in terms of its Fock components  $|\mu_n\rangle$ , where  $n$  in general is denumerably infinite. Each particular component  $|\mu_n\rangle$  contains a fixed number  $N_n$  of constituent quanta, the  $i^{\text{th}}$  of which has rest mass  $m_i$  and momentum  $k_i^\mu$  (out of the total momentum  $P^\mu$ ). The kinematics may alternatively be described in terms of longitudinal boost-invariant quantities  $x_i \equiv k_i^+/P^+$  ( $0 \leq x_i \leq 1$ ) and  $\mathbf{k}_{\perp i}$ , and helicities  $\lambda_i$ , so that

$$\sum_{i=1}^{N_n} x_i = 1, \quad \sum_{i=1}^{N_n} \mathbf{k}_{\perp i} = \mathbf{P}_\perp, \quad (4)$$

and, working in the *intrinsic frame*, in which  $\mathbf{P}_\perp = 0$ ,

$$k_i^\mu = \left( x_i P^+, \mathbf{k}_{\perp i}, \frac{m_i^2 + \mathbf{k}_{\perp i}^2}{x_i P^+} \right). \quad (5)$$

Using the completeness of the states  $|\mu_n\rangle$ , the decomposition then reads

$$\begin{aligned} |\Psi\rangle &\equiv \sum_n \int [d\mu_n] |\mu_n\rangle \langle \mu_n | \Psi; M, P^+, \mathbf{P}_\perp, S^2, S_z; h \rangle \\ &\equiv \sum_n \int [d\mu_n] |\mu_n\rangle \Psi_{n|h}(\mu), \end{aligned} \quad (6)$$

where the measure notation indicates an integration over values of all constituent  $x_i, \mathbf{k}_{\perp i}$ , subject to the constraints of Eq. (4). The functions  $\Psi_{n|h}(\mu)$ , where now  $h$  and  $\mu$  are shorthand for all the intrinsic and kinematic quantum numbers, respectively, of the Fock state  $n$ , are called the *component wave functions* of the state and are the central objects of interest in bound-state light-front calculations. The Hamiltonian expression Eq. (2) then becomes

$$\begin{aligned} \sum_{n'} \int [d\mu_{n'}] \langle \mu_n : x_i, \mathbf{k}_{\perp i}, \lambda_i | P^- | \mu_{n'} : x'_i, \mathbf{k}'_{\perp i}, \lambda'_i \rangle \\ \times \Psi_{n'|h}(x'_i, \mathbf{k}'_{\perp i}, \lambda'_i) \\ = \frac{M^2 + \mathbf{P}_\perp^2}{P^+} \Psi_{n|h}(x_i, \mathbf{k}_{\perp i}, \lambda_i), \end{aligned} \quad (7)$$

which is an exact infinite-dimensional integral equation for the component wave functions  $\Psi_{n|h}(\mu)$ . Although this expression has been derived from a full QFT with no approximations, one may identify it as the light-front

version of the Schrödinger equation. Specifically, the kinetic energy operator for the  $i^{\text{th}}$  component in the frame  $\mathbf{P}_\perp = 0$  reads

$$T_i = \frac{m_i^2 + \mathbf{k}_{\perp i}^2}{x_i}, \quad (8)$$

and the bound-state equation for two equal-mass valence particles interacting via the effective potential  $V_{\text{eff}}$  is described by the integral equation

$$\begin{aligned} \left( M^2 - \frac{m^2 + \mathbf{k}_\perp^2}{x(1-x)} \right) \psi(x, \mathbf{k}_\perp; \lambda_1, \lambda_2) \\ = \sum_{\lambda'_1, \lambda'_2} \int_D dx' d^2 \mathbf{k}'_\perp \langle x, \mathbf{k}_\perp; \lambda_1, \lambda_2 | V_{\text{eff}} | x', \mathbf{k}'_\perp; \lambda'_1, \lambda'_2 \rangle \\ \times \psi(x', \mathbf{k}'_\perp; \lambda'_1, \lambda'_2). \end{aligned} \quad (9)$$

The appearance of reciprocal powers of momenta in Eq. (2), which is the ultimate origin of the singularities at  $x = 0$  or  $1$  in Eq. (9), requires a careful regularization of numerical integrals. The domain  $D$  in Eq. (9) is defined by introducing a cutoff  $\Lambda$  on the parton transverse momentum  $\mathbf{k}_\perp$ ; in the equal-mass case, we choose [17]

$$\frac{m^2 + \mathbf{k}_\perp^2}{x(1-x)} \leq \Lambda^2 + 4m^2. \quad (10)$$

Instituting a momentum-space cutoff has the added effect of minimizing the influence of multiparticle Fock states. In principle, each sector of the theory (in our case, notably  $\mu\bar{\mu}$  and  $e\bar{e}$ ) can have an independent cutoff, but such choices must be motivated by the physical scales of the problem, and in any case the final results must eventually be insensitive to such particular choices. We discuss these issues in greater detail in Sec. VI.

For a gauge theory like QED, the light-cone gauge  $A^+ = 0$  is the most natural choice because it eliminates the spatial non-transverse modes. Using the equations of motion, one may then eliminate the  $A^-$  component in favor of the other fields in the theory; this inversion is subtle due to the existence of “zero modes” of  $A^+$ , but such modes are not expected to affect the spectrum of bound states in a crucial way [14]. The result is a fairly complicated but closed-form exact Hamiltonian that may be used to develop front-form Feynman rules [9, 17].

The Hamiltonian can be described by the sum of Feynman rules for a kinetic operator  $T$  and various types of interactions: *seagulls*  $S$  [including their normal-ordered *contractions*], which do not change particle number, *vertices*  $V$ , which change particle number by one, and *forks*  $F$ , which change particle number by two:

$$H_{\text{LC}} = T + S + V + F. \quad (11)$$

The exact form of each operator has been worked out and can be found in many places, *e.g.*, in Ref. [9]. The connection of the lowest Fock states by these interactions for true muonium is summarized in Table I.

Sector	$n$	0	1	2	3	4	5	6	7	8
$ \gamma\rangle$	0	•	V	V	•	F	F	•	•	•
$ e\bar{e}\rangle$	1	V	•	S	S	V	•	F	•	F
$ \mu\bar{\mu}\rangle$	2	V	S	•	S	•	V	•	F	F
$ \gamma\gamma\rangle$	3	•	S	S	•	V	V	•	•	•
$ e\bar{e}\gamma\rangle$	4	F	V	•	V	•	S	V	•	V
$ \mu\bar{\mu}\gamma\rangle$	5	F	•	V	V	S	•	•	V	V
$ e\bar{e}e\bar{e}\rangle$	6	•	F	•	•	V	•	•	•	S
$ \mu\bar{\mu}\mu\bar{\mu}\rangle$	7	•	•	F	•	•	V	•	•	S
$ \mu\bar{\mu}e\bar{e}\rangle$	8	•	F	F	•	V	V	S	S	•

TABLE I. The Hamiltonian matrix for two-flavor QED, where  $n$  labels Fock states. The vertex, seagull and fork interactions are denoted by V, S, F respectively. Diagonal matrix elements are indicated by •, and vanishing matrix elements by a •.

In order to reduce Eq. (7) to a finite-dimensional equation that can be solved numerically [in particular, the form Eq. (9)], the space of included Fock states  $\{|F\rangle\}$  must be truncated. The straightforward approach of using the fundamental interactions of  $\{|F\rangle\}$  alone and ignoring all others  $\{|\bar{F}\rangle\}$  is called the *Tamm-Dancoff method* [18, 19]. Unfortunately, this approach can easily sacrifice Lorentz covariance or gauge invariance; including the effect of higher Fock states  $\{|\bar{F}\rangle\}$  to restore the necessary structures is the aim of the *method of iterated resolvents* [20], which treats  $\{|\bar{F}\rangle\}$  as giving rise to effective interactions among the states  $\{|F\rangle\}$  [which, in Eq. (9), contribute to  $V_{\text{eff}}$ ]. Since only the complete theory (QED in our case) with arbitrarily complicated Fock states that are precisely related by the exact Lagrangian can uniquely specify the correct effective interaction, the iterated resolvents simply act to provide one minimal completion of the interaction, written exclusively in terms of  $\{|F\rangle\}$ .

### III. NUMERICAL SIMULATION ON THE LIGHT FRONT

To solve Eq. (9), one can discretize the momentum-space Fourier modes and solve the resulting eigenvalue problem on a finite grid (the DLCQ method). Discretization in  $(x, \mathbf{k}_\perp)$  space results in a asymmetric matrix, which significantly increases the computational effort, so one may instead use a set of variables  $(\mu, \theta, \phi)$  defined by

$$x = \frac{1}{2} \left( 1 + \frac{\mu \cos \theta}{\sqrt{m_i^2 + \mu^2}} \right), \quad (12)$$

$$\mathbf{k}_\perp = \mu(\sin \theta \cos \phi, \sin \theta \sin \phi, 0). \quad (13)$$

Using these variables, one may exchange  $\phi$  for the discrete quantum number  $J_z$  [14] and compute using only

$\mu, \theta$ . The new variable  $\mu$  can be considered an off-shell momentum, due to the relation

$$\frac{m_i^2 + \mathbf{k}_\perp^2}{x(1-x)} = 4(\mu^2 + m_i^2). \quad (14)$$

Since these coordinates depend upon the fermion mass  $m_i$ , different sets of  $\mu, \theta$  values result from the same sets of  $x$  and  $\mathbf{k}_\perp$  values in the two-flavor system.

To discretize, we utilize the Clenshaw-Curtis method (unlike Ref. [14], which used the Gauss-Legendre method) for  $\mu$ , to take advantage of its rapid convergence and reuse of quadrature points, and the Gauss-Chebyshev method for  $\theta$  to carefully sample the endpoints. The  $\mu$  range is  $[0, \frac{\Lambda_i}{2}]$ , where  $\Lambda_i$  is the momentum cutoff for flavor  $i$  (see Sec. VI), and  $\cos \theta \in [-1, 1]$ . To allow for values  $\Lambda_i \rightarrow \infty$ , we remap the interval to one  $\in [0, 1]$  via a weighting

$$f(\mu) = \frac{1}{1 + \mu}, \quad (15)$$

where  $\mu$  here is expressed in units of the Bohr momentum  $\alpha m_i/2$ . With reference to Eq. (12), if one fixes the cutoff  $\Lambda_i$  and increases the number of sampling points  $N_\mu$ , this mapping  $f$  then places more grid points at low  $\mu$  to better sample the wave function around  $x = \frac{1}{2}$ , and high  $\mu$  to better sample around  $x = 0, 1$ . From this scheme, one sees that four numbers essentially determine the quality of numerical calculation: the number of sampling points  $N_\mu$  and  $N_\theta$ , and the momentum cutoffs  $\Lambda_\mu$  and  $\Lambda_e$ . In cases where the number of sampling points  $N_\mu, N_\theta$  are set equal, we write  $N_\mu = N_\theta = N$ .

The  $1/q^2$  singularity introduced by the Coulomb interaction, where  $\mathbf{q}$  is the momentum transfer, is handled by the same *counterterm method* as described in Ref. [14] and first implemented in Ref. [12]: The sum over discrete matrix elements near the Coulomb singularity is performed by subtracting from the numerator a function that reduces the overall degree of divergence of the sum, thus making it more rapidly convergent. In order to obtain an identity, one must add back the term that was subtracted; however, the corresponding expression in this case is realized as integral rather than a sum, which can be numerically evaluated rather efficiently. The only necessary modification in the two-flavor case is to use separate counterterms in each flavor sector.

### IV. TRUE MUONIUM MODEL

Our model simply uses QED with two fermion flavors, the electron  $e$  and the muon  $\mu$ , but in which the “electron” is dramatically heavier than its physical value of  $m_e/m_\mu \simeq 4.8 \cdot 10^{-3}$ , in order to explore the effect of the extra flavor sector beyond a simple “scaled-up” version of positronium. Nevertheless, the condition  $m_e < m_\mu$  is always imposed, and as mentioned above, we set  $\alpha = 0.3$

to enhance the effects of the extra sector. In this basis, one can express the state of all possible charge-zero, lepton family-number zero wave functions defined by:

$$|\Psi\rangle = \psi_{\mu\bar{\mu}}|\mu\bar{\mu}\rangle + \psi_{e\bar{e}}|e\bar{e}\rangle + \psi_{\gamma}|\gamma\rangle + \psi_{\mu\bar{\mu}\gamma}|\mu\bar{\mu}\gamma\rangle + \psi_{e\bar{e}\gamma}|e\bar{e}\gamma\rangle + \dots \quad (16)$$

The full physical problem would require not only decreasing  $m_e$  and  $\alpha$ , but also including hadronic polarization function corrections to the photon propagators.

In this initial model of true muonium, we extend the Fock space considered in Refs. [14, 21–23] to include a second flavor of fermions:  $|\mu\bar{\mu}\rangle$ ,  $|\mu\bar{\mu}\gamma\rangle$ ,  $|e\bar{e}\rangle$ ,  $|e\bar{e}\gamma\rangle$ , and  $|\gamma\rangle$ . Through a proper choice of effective interactions [24], one can truncate the Fock space at these states and neglect other Fock states such as  $|\gamma\gamma\rangle$  or  $|\mu\bar{\mu}e\bar{e}\rangle$  in a self-consistent way. The  $|e\bar{e}\rangle$  states are of particular interest because their continuum states constitute the dominant decay mode of the  $^3S_1$  ( $C = -1$ ) states of true muonium. Furthermore, its inclusion in the numerical simulation (along with  $|e\bar{e}\gamma\rangle$ ) is straightforward because it requires no conceptual innovation beyond that used to study the  $|\mu\bar{\mu}\rangle$  and  $|\mu\bar{\mu}\gamma\rangle$  states; the greatest complication is that the matrices to be diagonalized become much larger, increasing computation time.

Solving for the eigenstates of  $H_{LC}$  with this limited Fock space nonetheless gives the bound states of positronium ( $e\bar{e}$ ) and true muonium ( $\mu\bar{\mu}$ ), as well as the continuum states of  $\gamma$ ,  $e\bar{e}$ , and  $\mu\bar{\mu}$ , exactly (up to the effects due to the neglected higher-order Fock states). The output of this calculation is the wave functions of various helicity states for  $|\mu\bar{\mu}\rangle$  and  $|e\bar{e}\rangle$  components  $\psi$  in the form of Eq. (9), *i.e.*, with the  $|\gamma\rangle$  components folded into  $V_{\text{eff}}$  by means of the method of iterated resolvents.

## V. EFFECT OF THE $|e\bar{e}\rangle$ SECTOR

Proper inclusion of the front-form Fock states  $|e\bar{e}\rangle$  and  $|e\bar{e}\gamma\rangle$  should replicate the physics in instant form due to the inclusion of instant-form diagrams with an  $e^+e^-$  pair and a  $\gamma$ , such as vacuum polarization due to electrons in the single-photon annihilation channel (called VP-e-A in Ref. [25]). The importance of including both  $|e\bar{e}\rangle$  and  $|e\bar{e}\gamma\rangle$  states in our simulations is twofold.

First, the dominant decay channel for true muonium in  $^3S_1$  states is  $e^+e^-$  production, while the dominant decay channel for  $^1S_0$  ( $C = +1$ ) states is  $\gamma\gamma$ . Note that the well-known leading-order result for the  $^3S_1$ - $^1S_0$  hyperfine splitting,  $\Delta E = \frac{7}{12}m_\mu\alpha^4$  for true muonium, has been derived analytically in front form [26, 27], so that other physical effects sensitive to small  $\mu^+\mu^-$  separation such as  $\mu^+\mu^- \rightarrow \gamma \rightarrow e^+e^-$  should also be considered.

While including the  $|e\bar{e}\rangle$  state into our calculations requires essentially nothing but duplicating the  $|\mu\bar{\mu}\rangle$  states as  $|e\bar{e}\rangle$  and computing one new set of matrix elements (see Appendix), properly including a  $|\gamma\gamma\rangle$  state would require computing many new matrix elements, developing new

counterterms to regularize singular integrals, and properly renormalizing the photon mass terms that arise on the light front. We plan to address these issues in future work.

Second, Jentschura *et al.* [25] showed in instant form that VP-e-A is the second-largest correction to the hyperfine splitting in true muonium. The only correction that is larger in instant form arises from vertex corrections, which are partly incorporated in front form through the inclusion of  $|\mu\bar{\mu}\gamma\rangle$  states, but can be fully treated only through proper renormalization. Furthermore, Ref. [25] finds the energy shifts arising from the  $|\gamma\gamma\rangle$  states to be several times smaller than those from either VP-e-A or vertex corrections. The calculations of Ref. [25] rely upon the asymptotic behavior of the vacuum polarization, which for true muonium is the limit of  $m_e/m_\mu \ll 1$ . In our case of  $m_e/m_\mu = O(1)$ , one might expect significant corrections to the asymptotic behavior. To find the effect of these corrections, one can compute the exact correction due to VP-e-A without the asymptotic approximation. As first shown in [28], the leading-order radiative correction to the QED particle-antiparticle bound-state energy spectrum due to a virtual fermion loop coupling to the electromagnetic field with amplitude  $\varphi_0$  (which, in the nonrelativistic limit, is just the wave function) is

$$\begin{aligned} \Delta E_{VP} &= \frac{\pi\alpha}{m_i^2} \left(1 - \frac{4\alpha}{\pi}\right) \bar{\Pi}^R(4m_i^2) |\varphi_0|^2 \langle \mathbf{S}^2 \rangle + O(\alpha^6) \\ &= \frac{\alpha^4 m_i}{4n^3} \left(1 - \frac{4\alpha}{\pi}\right) \bar{\Pi}^R(4m_i^2) + O(\alpha^6), \end{aligned} \quad (17)$$

where  $m_i$  is the mass of the bound fermion,  $\bar{\Pi}^R(q^2)$  is the renormalized polarization function, and  $\mathbf{S}^2$  is the total spin Casimir operator. In the second line we have specialized to the  $n^3S_1$  state, for which  $|\varphi_0|^2 = m_i^3 \alpha^3 / 8\pi n^3$  is the nonrelativistic squared wave function at the origin, and  $\langle \mathbf{S}^2 \rangle = 2$ . The exact form of the one-loop vacuum polarization function is

$$\bar{\Pi}^R(q^2) = \frac{\alpha}{3\pi} \left[ -\frac{5}{3} - \frac{4m_f^2}{q^2} + \left(1 + \frac{2m_f^2}{q^2}\right) f(q^2) \right], \quad (18)$$

where  $m_f$  is the mass of the loop fermions, and the form of  $f(q^2)$  depends upon whether  $q^2$  is spacelike or timelike and its size compared to  $4m_f^2$ . In the region  $4m_f^2 < q^2$ , *e.g.*, for true muonium with electron-loop corrections, one finds

$$f(q^2) = \sqrt{1 - \frac{4m_f^2}{q^2}} \ln \left( \frac{1 + \sqrt{1 - \frac{4m_f^2}{q^2}}}{1 - \sqrt{1 - \frac{4m_f^2}{q^2}}} \right) - i\pi \sqrt{1 - \frac{4m_f^2}{q^2}}, \quad (19)$$

where the imaginary term signals the possibility for decay. Inserting Eqs. (18)–(19) into Eq. (17), taking the  $m_e \rightarrow 0$  limit, and dropping the  $O(\alpha^6)$  terms, we reproduce Eq. (26) of [25], which we express slightly differently

as

$$\Delta E_{\text{VP}}(n^3S_1) = \frac{m_\mu \alpha^5}{4\pi n^3} \left[ \frac{1}{3} \ln \left( \frac{4m_\mu^2}{m_e^2} \right) - \frac{5}{9} - \frac{i\pi}{3} + O \left( \frac{m_e^2}{4m_\mu^2}, \alpha \right) \right]. \quad (20)$$

In typical cases considered here ( $m_e/m_\mu \sim 0.1$ – $0.8$ ), this expansion predicts relative corrections to the asymptotic form of order 10%, so the complete formulas [Eqs. (17)–(19)] are retained for our numerical results.

In order to compare our results to those of instant-form perturbation theory calculations, we compare shifts in  $M^2$ :

$$\begin{aligned} \Delta M^2 &\equiv M_{\mu\mu}^2 - M_0^2 \\ &= (2m_\mu + B + \Delta E)^2 - (2m_\mu + B)^2, \end{aligned} \quad (21)$$

where  $M_{\mu\mu}^2$  is the squared mass of our model true muonium including the  $|e\bar{e}\rangle$  component, while  $M_0^2$  is the squared mass neglecting the electron Fock states,  $\Delta E$  is the total binding energy due to the presence of the  $|e\bar{e}\rangle$  states, and  $B$  is the remaining binding energy terms of the atom. In Sec. VII we examine how well taking  $\Delta E = \Delta E_{\text{VP-e-A}}$ , where the latter refers to the original instant-form expression of Eq. (17), matches the light-front results.

## VI. CUTOFF AND RENORMALIZATION ISSUES

In front form, the most common renormalization scheme for two-body systems is the covariant cutoff approach of Lepage and Brodsky [17]:

$$\frac{m^2 + \mathbf{k}_\perp^2}{x(1-x)} \leq \Lambda^2 + 4m^2. \quad (22)$$

Unfortunately, in any but the simplest models, this formulation does not properly regularize the Hamiltonian as new sectors are added. More recent attempts to utilize other renormalization schemes include Pauli-Villars [29, 30] and Hamiltonian flow [31, 32] techniques, and methods with sector-dependent counterterms [33, 34]. The first steps to study positronium using the basis light-front approach have appeared very recently [35].

For the purposes of this work, we take the simplest possible renormalization scheme by defining two covariant cutoffs via Eq. (22):  $\Lambda_\mu$  for the muon sector and  $\Lambda_e$  for the electron sector. Since Eqs. (14), (22) identify  $\Lambda$  as a maximum off-shell momentum for the parton of mass  $m$ , physical considerations lead one to expect that  $\Lambda$  should be larger for lighter components of a single bound-state system. In the true muonium case, choices such as  $\Lambda_e^2 = \Lambda_\mu^2 + 4(m_\mu^2 - m_e^2)$  are natural, and this is the scheme adopted here. In particular,  $\Lambda_e$  should be chosen

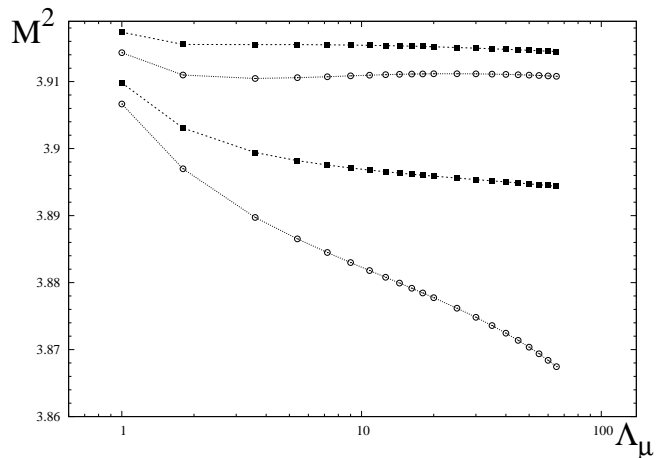


FIG. 1. Mass eigenvalues of  $n = 1$  true muonium states with  $J_z = 0$  ( $1^3S_1^0$  in top pair,  $1^1S_0^0$  in bottom pair) as a function of cutoff  $\Lambda_\mu$  for  $\Lambda_e^2 = \Lambda_\mu^2 + 4(m_\mu^2 - m_e^2)$ ,  $\alpha = 0.3$ ,  $m_e = \frac{1}{2}m_\mu$ ,  $N = 25$ .  $\Lambda_\mu$  is given in units of the muon Bohr momentum  $\alpha m_\mu/2$ . The ( $\circ$ ) points indicate the full result precisely following the methods of Ref. [14], and the ( $\blacksquare$ ) points indicate the result after the implementation of a subtraction (described in the text) of the amplitude responsible for poor ultraviolet behavior in  $1S_0$  channels.

significantly larger than  $\Lambda_\mu$ , or else the phase space for  $|e\bar{e}\rangle$  continuum states contributing to true muonium is inappropriately truncated, leading to numerical instabilities due to undersampling of physically significant amplitudes. This physically appropriate choice nevertheless leads to interesting numerical issues, as discussed in the next section.

To investigate the effect of this choice of cutoffs, we fix  $\Lambda_e$  as described above and vary  $1 \leq \Lambda_\mu \leq 65$  (in units of muon Bohr momentum  $\alpha m_\mu/2$ ). Results for the  $n = 1, 2$  eigenstates with  $m_e = \frac{1}{2}m_\mu$  can be seen in Figs. 1 and 2, respectively, which can be compared to Figs. 2.8 and 2.9 of Ref. [14], where the same study was performed for positronium. For an exact analogue to the results of Ref. [14], one should compare the lines in Fig. 1 with open-circle points directly to their analogues in the earlier work. Since rotational invariance is obscured in the front form, states studied in the numerical simulations are labeled by adding the  $J_z$  label, as in  $n^{2S+1}L_{J_z}^{J_z}$ .

The most striking feature of the initial (open-circle points) results in Fig. 1 is the strong dependence on the cutoff  $\Lambda_\mu$  of the  $1^1S_0$  mass eigenvalue compared to that of  $1^3S_1$  (A similar effect occurs for the  $2^1S_0$  mass eigenvalue). One may initially wonder whether this effect is due to an inappropriate handling of lepton mass renormalization. The full shift of the bound-state mass due to one-loop lepton mass renormalization in front form is

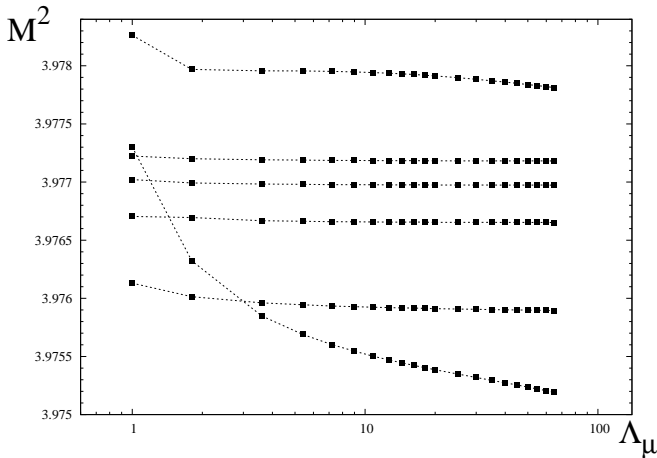


FIG. 2. Mass eigenvalues of  $n = 2$  true muonium states with  $J_z = 0$  (top to bottom:  $2^3S_1^0$ ,  $2^3P_2^0$ ,  $2^1P_1^0$ ,  $2^3P_1^0$ ,  $2^1S_0^0$ ) as a function of cutoff  $\Lambda_\mu$ . The numerical inputs and units of  $\Lambda_{e,\mu}$  are the same as in Fig. 1. The amplitude subtraction described in the text has been performed for all states here.

given by [12]

$$\Delta M^2 = \frac{\alpha}{2\pi} m^2 \left[ 3 \ln \left( \frac{\Lambda^2 + m^2}{m^2} \right) - \frac{\Lambda^2}{\Lambda^2 + m^2} \right] \times \left( \frac{1}{x} + \frac{1}{1-x} \right). \quad (23)$$

This expression is obtained from the sum of loop and contraction diagrams; as is well known (*e.g.*, see [9]), the individual loop diagrams that give the renormalization constants  $Z_2$  or  $Z_1$  in light-front form carry momentum dependence, but the Ward identity guarantees that their sum does not, allowing one to adopt an on-shell renormalization scheme in which the input  $\alpha$  and  $m$  values are given by the physical ones. Since the higher-order corrections not given here must necessarily subtract the  $\ln \Lambda$  divergence of Eq. (23) but generally produce additional corrections, one may choose to remove the divergence in a variety of ways. The work of Refs. [12, 14] advocates simply taking  $\Delta M^2 = 0$ . To gauge the effect of other choices, we consider either subtracting from the bracketed term of Eq. (23) only the  $\ln(\Lambda^2/m^2)$  portion, or the  $O[(m^2)^0]$  correction as well. In the latter case, the bound-state eigenvalues  $M^2$  change by less than 1 part in  $10^4$  by the time  $\Lambda_\mu$  is as small as  $2m_\mu$ . We therefore also opt for the simple choice  $\Delta M^2 = 0$  in this work.

We also note that the derivation of Eq. (23) neglects one diagram, in which the leptons exchange an “instantaneous” photon in the presence of a spectator photon, because it is non-diagonal in the single-lepton spins and momenta, and therefore gives rise to a self-mass correction of the atom that is not just a single-lepton mass renormalization. Certainly, such an effect could be included as an  $O(\alpha^2)$  perturbative correction.

Indeed, it is hard to imagine how simple lepton mass renormalization would treat the  $1S_0$  states so differently

from the others. This phenomenon was noted as early as Ref. [12]. Since the subsequent work of Ref. [14] improved the numerical quality of the  $C = -1$   $3S_1$  states by the inclusion of the Fock state  $|\gamma\rangle$ , one may expect the inclusion of  $|\gamma\gamma\rangle$  to improve the  $C = +1$   $1S_0$  states. We will present analysis of this effect in the future [16], but for the present adapt a regularization first suggested in Ref. [12]: The strong dependence of  $1S_0$  states on  $\Lambda$  can be traced to a portion of the matrix element between lepton antiparallel-helicity states (called  $G_2$  in App. F.3 of Ref. [14]) that approaches a constant as  $k_\perp \equiv |\mathbf{k}_\perp|$  or  $k'_\perp \equiv |\mathbf{k}'_\perp| \rightarrow \infty$  and therefore produces  $\delta$  function-like behavior in configuration space. Including such dependence imposes a singular ultraviolet behavior on the system, and therefore it must be regularized; Ref. [12] chose simply to delete this term from their calculations. However, we choose to subtract only its limit as  $k_\perp$  or  $k'_\perp \rightarrow \infty$ , which retains part of the term (including  $x$  and  $x'$  dependence). Again, this subtraction scheme is designed only to remove strong  $\Lambda$  dependence in  $1S_0$  states that the explicit inclusion of the  $|\gamma\gamma\rangle$  state must eventually address. The effect of this subtraction is shown as lines in Figs. 1,2 with filled square points, and demonstrates a great improvement in the stabilization of the  $\Lambda$  dependence of  $1S_0$  states, with fairly minimal changes to that of other states. The subtraction for the  $2^1S_0$  state is not shown in Fig. 2, but it amounts to a decrease in the  $\Lambda_\mu$  dependence by over a factor of 10.

We explore the sensitivity of the results to varying  $\Lambda_e$  in Fig. 3, where the mass eigenvalues of the  $1^1S_0$  and  $1^3S_1$  states are reported as functions of  $\Lambda_e$  in units of the muon Bohr momentum  $\alpha m_\mu/2$ . That is,  $\Lambda_e \simeq 11.6$  corresponds to the value used in Figs. 1,2. The results are quite insensitive to larger  $\Lambda_e$ , which means that allowing for greater off-shell momentum in the  $|e\bar{e}\rangle$  sector than in our simple prescription has very little impact on the true muonium spectrum. On the other hand, decreasing  $\Lambda_e^2$  below  $\Lambda_\mu^2 + 4(m_\mu^2 - m_e^2)$  (not depicted here) reveals strong fluctuations in the dependence of mass eigenvalues upon  $\Lambda_e$ , which we attribute to an undersampling of the continuum  $|e\bar{e}\rangle$  states with invariant mass below the full true muonium bound-state mass; the analogous effect in a hadronic physics calculation would be interpreted as a failure of quark-hadron duality due to insufficient phase space allowed for lighter components of the hadron bound state.

## VII. RESULTS

Using a version of the code in Ref. [14] modified as discussed above, we compute the entire bound-state spectrum of true muonium and positronium including valence Fock states of both  $|\mu\bar{\mu}\rangle$  and  $|e\bar{e}\rangle$  for  $J_z = -3, -2, \dots, +3$  (*e.g.*, Fig. 4), taking  $\alpha = 0.3$ ,  $m_e = \frac{1}{2}m_\mu$ ,  $\Lambda_\mu = 10\alpha m_\mu/2 \simeq 1.5m_\mu$ , and  $\Lambda_e = [\Lambda_\mu^2 + 4(m_\mu^2 - m_e^2)]^{1/2} \simeq 15.3\alpha m_\mu/2 \simeq 2.3m_\mu$ .

From Fig. 4, we see that the true muonium spectrum is

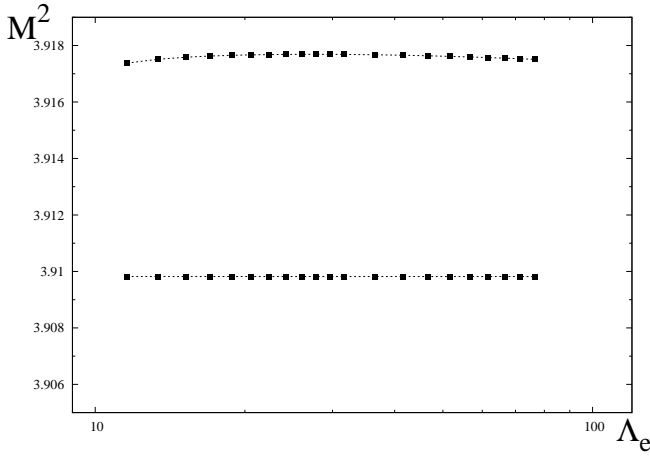


FIG. 3. Mass eigenvalues of  $n = 1$  true muonium states with  $J_z = 0$  ( $1^3S_1^0$  at top,  $1^1S_0^0$  at bottom) as a function of cutoff  $\Lambda_e$  in units of the muon Bohr momentum  $\alpha m_\mu/2$ , with  $\Lambda_\mu = 1$  in these units,  $\alpha = 0.3$ ,  $m_e = \frac{1}{2}m_\mu$ ,  $N = 25$ .

nearly identical to that found in [14]. The shifts caused by the inclusion of the  $e\bar{e}$  sector are smaller than can be resolved in this plot. Likewise, the positronium spectrum indicates multiplets with the expected multiplicities and ordering.

True muonium presents an extremely intriguing physical situation not typically encountered in light-front studies, and particularly not in light-front positronium studies: In the invariant mass range  $4m_e^2 < M^2 < 4m_\mu^2$ , the  $|\mu\bar{\mu}\rangle$  component is bound but the  $|e\bar{e}\rangle$  component forms a continuum. The invariant mass  $M_S$  of the  $|e\bar{e}\rangle$  state satisfies the constraint

$$M_S^2 = \frac{m_e^2 + \mathbf{k}_\perp^2}{x(1-x)}, \quad (24)$$

but is otherwise unconstrained. Representing such states in the DLCQ formulation presents interesting numerical challenges, analogous to representing band structures in solid-state systems by closely-spaced discrete energy levels. Even so, since the two flavor sectors can only interact through the single-photon annihilation channel, the only true muonium states in this model affected by the inclusion of  $|e\bar{e}\rangle$  are those with  $|J_z| \leq 1$  [14]. Denoting the bound-state mass-squared eigenvalue before and after including the  $e\bar{e}$  states as  $M_0^2$  and  $M_{\mu\mu}^2$ , respectively, Fig. 5 plots the magnitudes of the mass shifts  $\Delta M^2 \equiv M_{\mu\mu}^2 - M_0^2$  of  $J_z = 0$  true muonium states as a function of  $m_e$  in the  $n = 1, 2, 3$  energy levels.

Although the results may seem noisy in  $m_e$ , one must first note that the shifts  $\Delta M^2$  are so small that they at no point lead to a level crossing, and moreover, a trend is clearly visible that suggests the shifts decrease quickly with increasing principal quantum number  $n$  (approximately as  $1/n^3$ , see below). For the  $J_z = 0$  case,  $n^3S_1^0$  are the only states affected by the new sector in a numerically significant way, in agreement with front-form pre-

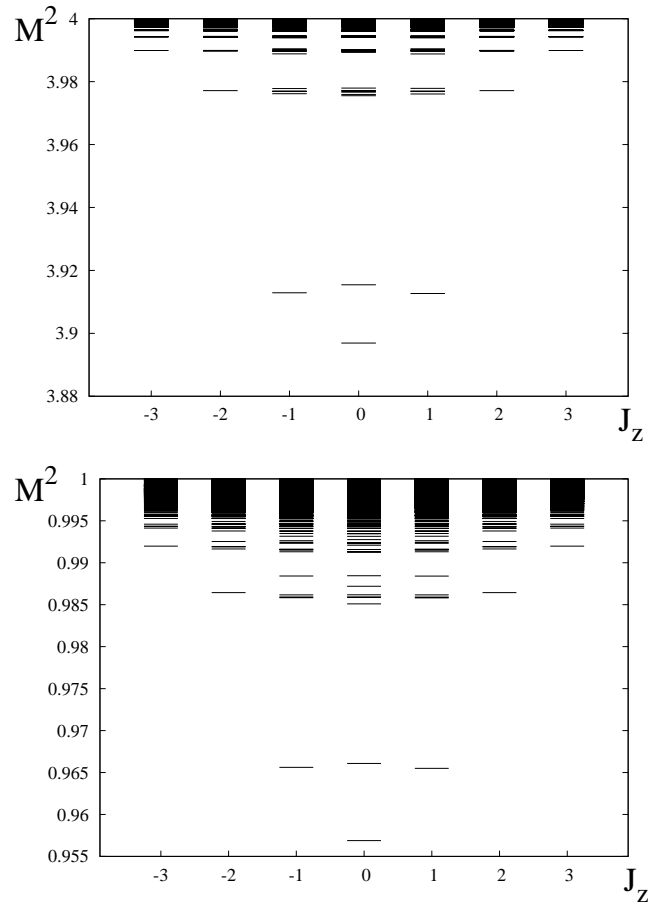


FIG. 4. Spectrum of (top) true muonium and (bottom) positronium with  $J_z = -3, -2, \dots, +3$ . The spectra are calculated using  $\alpha = 0.3$ ,  $m_e = \frac{1}{2}m_\mu$ ,  $\Lambda_\mu = 10\alpha m_\mu/2$ ,  $\Lambda_e = [\Lambda_\mu^2 + 4(m_\mu^2 - m_e^2)]^{1/2} \simeq 15.3\alpha m_\mu/2$ ,  $N = 25$ . The mass-squared eigenvalues  $M_n^2$  are expressed in units of  $m_\mu^2$ .

dictions [14]. One finds in the  $|J_z| = 1$  cases (not plotted here) the  $P$  states are also affected, but at a much lower level, and that the mass shifts for states differing only in  $J_z$  are not the same, reflecting that rotational invariance in the light-front calculation at finite numerical accuracy is not entirely restored.

The reason for the fluctuations in Fig. 5 is just as interesting as the results themselves. As indicated above, the  $|e\bar{e}\rangle$  continuum states near the  $|\mu\bar{\mu}\rangle$  bound states, (which lie just below  $M^2 = 4m_\mu^2$ ) are simulated numerically in DLCQ as clusters of discrete energy levels rather than a true continuum. The location in  $M^2$  of these clusters is determined by  $\mu$  [Eq. (14)], with the number of such clusters and the size of gaps between them determined largely by  $N_\mu$ . The density of energy levels within each cluster is determined by  $N_\theta$ , but we also note that the spacing of the levels within each cluster is not entirely uniform, being more dense at larger values of  $M^2$ .

One expects that simply increasing the values of  $N_\mu$  and  $N_\theta$  in the simulations must eventually suppress the



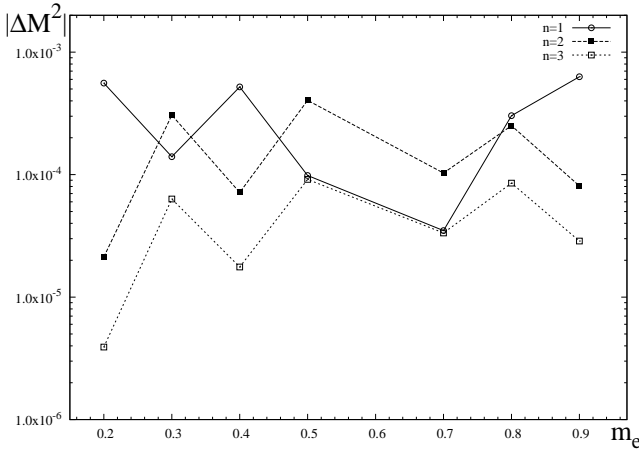


FIG. 5. Eigenvalue shifts  $\Delta M^2 \equiv M_{\mu\mu}^2 - M_0^2$  (in units of  $m_\mu^2$ ) for the  $n \leq 3$ ,  $J_z = 0$  triplet states of true muonium as functions of  $m_e$ , for  $\alpha = 0.3$ ,  $\Lambda_\mu = \alpha m_\mu/2$ ,  $\Lambda_e = [\Lambda_\mu^2 + 4(m_\mu^2 - m_e^2)]^{1/2} \simeq 11.6\alpha m_\mu/2$ , and values of  $N$  are adjusted as described in the text. From top to bottom, the states are  $1^3S_1^0$ ,  $2^3S_1^0$ , and  $3^3S_1^0$ .

numerical artifacts associated with the discretization. However, for the moderate values ( $N_\mu, N_\theta < 50$ ) used here, several features make the analysis more complicated: First, the larger value of the cutoff  $\Lambda_e$  compared to  $\Lambda_\mu$  (see Sec. VI) allows for a substantial phase space to be available to the  $|e\bar{e}\rangle$  continuum states, only some of which overlap with the  $|\mu\bar{\mu}\rangle$  bound states, and this issue is exacerbated as  $\Lambda_e$  increases; in other words, only some of the  $|e\bar{e}\rangle$  clusters overlap with the  $|\mu\bar{\mu}\rangle$  states, and simply increasing  $N_\mu$  does not directly alleviate this fact. Related to this point is the nonlinear nature of the mapping Eq. (15), which was designed to guarantee a sufficient sampling of points up to  $\mu = \frac{\Lambda_e}{2}$ , but does not necessarily suitably sample the region near the  $|\mu\bar{\mu}\rangle$  bound states.

The discrete sampling of these continuum states has a noticeable effect on the shifts  $\Delta M^2$ . Quite generally, we find that a given  $|\mu\bar{\mu}\rangle$  bound state prior to the inclusion of electrons undergoes a shift in  $\Delta M^2$  toward the energy levels of the  $|e\bar{e}\rangle$  states in the nearest clusters. Clearly, such an effect is a numerical artifact since the true  $|e\bar{e}\rangle$  spectrum is continuous, and the shift can be pronounced if the numerical simulation is such as to produce no cluster of  $|e\bar{e}\rangle$  states near the original  $|\mu\bar{\mu}\rangle$  bound state. We report only results from simulations in which the  $|\mu\bar{\mu}\rangle$  state lies within an  $|e\bar{e}\rangle$  cluster; guaranteeing that this scenario occurs requires a delicate balancing of the parameters  $m_e$ ,  $\Lambda_e$ ,  $N_\mu$ , and attention to the nature of the mapping function  $f(\mu)$ . Even in the case that a  $|\mu\bar{\mu}\rangle$  state lies neatly within an  $|e\bar{e}\rangle$  cluster, one must note that not every  $|e\bar{e}\rangle$  state has the same quantum numbers as the  $|\mu\bar{\mu}\rangle$  state and can mix with it. All of these effects must be taken into account in understanding the nature of results like Fig. 5; nevertheless, the fact remains that

broad trends of definite physical significance can still be identified.

For example, the addition of the  $|e\bar{e}\rangle$  component should lead to a modification of the Lamb shift (by which we mean the sum of all radiative corrections) proportional to a power of the principal quantum number  $n$ . While the specific quantitative values of these shifts show some sensitivity to the inputs, one might expect their ratios for different states for any given set of simulation parameters  $m_e$ ,  $\Lambda_e$ , and  $N$  to be less sensitive. To study the Lamb shift modifications, we take the ratio of the mass shifts for different  $n$  for  $^3S_1$  states. We define the ratio  $r_{nn'}$  for  $n' > n$  via

$$r_{nn'} \equiv \frac{\Delta M_n^2}{\Delta M_{n'}^2}. \quad (25)$$

Taking the average of  $r_{nn'}$  over all  $m_e$  values used for the computations, we determine the leading-order dependence  $\Delta M_n^2 \propto n^{-\beta}$  from the relation

$$\ln(r_{nn'}) = -\beta \ln\left(\frac{n}{n'}\right). \quad (26)$$

The results are presented in Table II. We find that  $\beta \approx 3$  for  $^3S_1$  states, which agrees with instant-form perturbation theory calculations of Lamb shifts [36].

$^{2S+1}L_J^{J_z}$	$\beta$		
$n, n'$	1, 2	1, 3	2, 3
$^3S_1^0$	$2.97 \pm 0.09$	$3.3 \pm 0.3$	$3.3 \pm 0.3$
$^3S_1^{-1}$	$3.2 \pm 0.2$	$3.3 \pm 0.2$	$3.6 \pm 0.4$

TABLE II. The exponent  $\beta$  defined in Eq. (26) for different states over the range  $0.1 \leq m_e/m_\mu \leq 0.9$ . Errors are estimated from the variation in  $m_e$  and  $N$ .

As discussed in Sec. V, one can compare the results of our simulations to the predictions of nonrelativistic instant-form results through Eqs.(17)–(21). Consider, for example,  $\Delta M^2$  of  $1^3S_1^0$ . Even though the individual simulations at particular fixed choices of  $N_{\mu,\theta}$  for a given  $m_e$  do not rapidly converge to a single fixed value at the moderate values of  $N_{\mu,\theta}$  used here, if one restricts to simulations in which the  $|\mu\bar{\mu}\rangle$  state lies within a  $|e\bar{e}\rangle$  cluster for the given  $m_e$ , the eigenvalue shifts then lie in constrained ranges and one may extract meaningful results by statistically averaging over the results of these simulations, as exhibited in Fig. 6. These light-front numerical results are seen in fact to agree fairly well with the instant-form result, with a few important caveats: First, the uncertainties become much larger for the smallest values of  $m_e$  (specifically seen in  $m_e = 0.2m_\mu$  in Fig. 6), due to the increasing difficulty of properly sampling the  $|e\bar{e}\rangle$  clusters for small  $m_e$  (on the other hand, simulations using smaller values of  $\alpha$  are not problematic, and simply serve to decouple the true muonium and positronium spectra). Second, the tiny uncertainties at  $m_e = 0.5m_\mu$  and  $0.7m_\mu$  reflect the accidental tendency of  $|e\bar{e}\rangle$  clusters

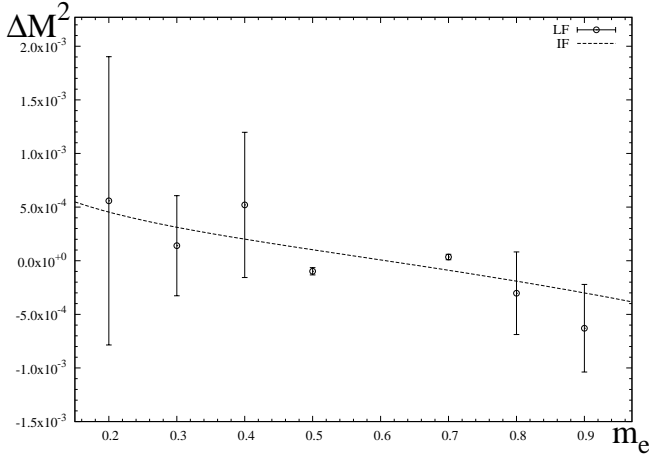


FIG. 6. Eigenvalue shifts  $\Delta M^2 \equiv M_{\mu\mu}^2 - M_0^2$  (in units of  $m_\mu^2$ ) for  $1^3S_1^0$ . The dashed line IF is the instant-form prediction from Eq. (21), using the nonrelativistic wave function, while the light-front (LF) points are obtained by taking  $\alpha = 0.3$ ,  $\Lambda_\mu = \alpha m_\mu/2$ ,  $\Lambda_e^2 = [\Lambda_\mu^2 + 4(m_\mu^2 - m_e^2)]^{1/2} \simeq 11.6\alpha m_\mu/2$ , and averaging over the results using several suitable values of  $N$ , as described in the text.

to appear in the region of the  $1^3S_1^0 |\mu\bar{\mu}\rangle$  state. Moreover, from the formal point of view, the instant-form and light-front calculations have three significant differences. First, the instant-form result here represents only the real part of the energy shift due to vacuum polarization and ignores, for example, vertex corrections. In front form, all of these effects are combined together when one includes explicit  $|e\bar{e}\rangle$  and  $|e\bar{e}\gamma\rangle$  states. Second, vacuum polarization diagrams in instant form contribute to the renormalization of the coupling constant, an effect not taken into account in this simple model. Finally, a result like Eq. (20) uses only the simplest expression for the nonrelativistic wave function; instant-form calculations that improve upon the nonrelativistic wave function result appear in, *e.g.*, Refs. [37, 38]. Nevertheless, the level of agreement in Fig. 6 is gratifying.

Inclusion of the  $|e\bar{e}\rangle$  sector also changes the wave functions. One expects that any true muonium bound state contains some component of electron-positron continuum states. The interaction of these states with the true muonium should lead to a modification of the wave functions by means of the  $|e\bar{e}\rangle$  component. As noted above, the  $1^3S_1^0$  wave function is expected to be affected the most by the inclusion of the  $|e\bar{e}\rangle$ . In Fig. 7 we plot the probability density of the components of the  $1^3S_1^0$  state of true muonium using a particular set of parameters. Noting the relative scales, one sees that the antiparallel components dominates the state. As expected for a bound state, the  $\mu\bar{\mu}$  pair is localized near  $x = \frac{1}{2}$  and  $k_\perp \equiv |\mathbf{k}_\perp| = 0$ .

Again, the  $|e\bar{e}\rangle$  wave function components of this state are expected to appear as continuum states, since the invariant mass  $M^2 > 4m_e^2$ . From Fig. 7, one sees that the  $e^+e^-$  component is sharply peaked along the curve

given by Eq. (24), where  $M_S^2$  is now also the invariant mass  $M^2$  of the  $1^3S_1^0$  state; the functional sharpness of such components suggests how difficulties in numerical sampling can occur, as discussed in Sec. VI and seen in Fig. 5. Additionally, one sees that the fermionic nature of the electrons is manifested most visibly in the parallel helicity component, where at  $x = \frac{1}{2}$  the probability is heavily suppressed. One also sees that, in agreement with the muonic components, the antiparallel component numerically dominates.

Integrating over the coordinates  $x, k_\perp$ , we compile in Table III the integrated probability for each component. From this exercise, we find the surprising result that the antiparallel electronic components contribute more to the wave function than the parallel muonic component. The large uncertainties in the integrated probabilities for the continuum components arise from their sensitive dependence upon  $\Lambda_e$  and  $N$  discussed in Sec. VI.

Sector	$\int dx d^2\mathbf{k}_\perp P(x, k_\perp)$
$ \mu\bar{\mu}, \uparrow\uparrow\rangle$	$(3.0 \pm 0.4) \times 10^{-6}$
$ \mu\bar{\mu}, \uparrow\downarrow\rangle$	$0.49 \pm 0.01$
$ e\bar{e}, \uparrow\uparrow\rangle$	$\approx 10^{-7} - 10^{-6}$
$ e\bar{e}, \uparrow\downarrow\rangle$	$\approx 10^{-3} - 10^{-2}$

TABLE III. Integrated probability for each sector in the true muonium  $1^3S_1^0$  state. Due to the parity invariance of QED, sectors with both helicities flipped have identical probability [*e.g.*,  $P(|\mu\bar{\mu}, \uparrow\uparrow\rangle) = P(|\mu\bar{\mu}, \downarrow\downarrow\rangle)$ ], so the explicit numbers in this table should add to  $\frac{1}{2}$ . The parameters used are  $\alpha = 0.3$ ,  $m_e = \frac{1}{2}m_\mu$ ,  $\Lambda_\mu = 10\alpha m_\mu/2$ ,  $\Lambda_e = [\Lambda_\mu^2 + 4(m_\mu^2 - m_e^2)]^{1/2} \simeq 15.3\alpha m_\mu/2$ ,  $N = 37$ . Uncertainties are estimated by varying  $N$ .

## VIII. DISCUSSION AND CONCLUSIONS

In this paper, we have computed the light-front wave functions of true muonium, using a simple model of two-flavor QED that includes a limited number (5) of explicit Fock states. Using this model, we have seen that corrections from  $|e\bar{e}\rangle$  have a noticeable effect on true muonium states. The probability density for the first excited state of true muonium, the triplet  $1^3S_1$  with  $J_z = 0$ , was determined and the integrated probability for each valence Fock-space component was computed. If  $m_e$  is taken to be a substantial fraction of  $m_\mu$  and the fine structure constant is taken large ( $\alpha = 0.3$ ), then the  $|e\bar{e}\rangle$  states constitute as much as  $O(10^{-2})$  of the true muonium eigenstates.

For a more accurate model, three critical Fock states must also be included:  $|\gamma\gamma\rangle$ , which dominates the decay of singlet states of true muonium (and in particular should have a pronounced effect on  $1S_0$  wave functions), and the pair of states  $|\mu\bar{\mu}e\bar{e}\rangle$  and  $|\mu\bar{\mu}\mu\bar{\mu}\rangle$ , which provide crucial contributions to the vacuum polarization corrections. To integrate these states into a model, a

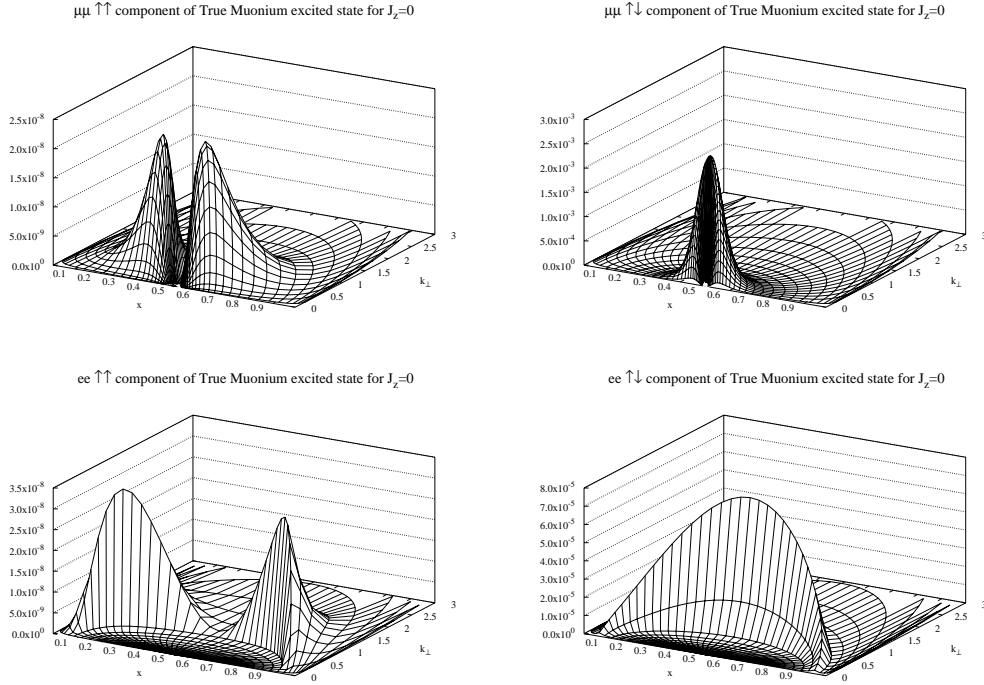


FIG. 7. The first triplet state ( $1^3S_1^0$ ) probability density of the (top left) parallel-helicity muonic, (top right) antiparallel-helicity muonic, (bottom left) parallel-helicity electronic, and (bottom right) antiparallel-helicity electronic components of true muonium with  $J_z = 0$ , as functions of  $x$  and  $k_\perp$ , for  $\alpha = 0.3$ ,  $m_e = \frac{1}{2}m_\mu$ ,  $\Lambda_\mu = 10\alpha m_\mu/2$ ,  $\Lambda_e^2 = \Lambda_\mu^2 + 4(m_\mu^2 - m_e^2)$ , and  $N = 37$ .

proper renormalization of the Hamiltonian is necessary. Methods of interest that have been developed to carry out the renormalization include using Pauli-Villars regulators [29, 30], the Hamiltonian-flow approach [31, 32], methods with sector-dependent counterterms [33, 34], and the basis light-front approach [35]. Moreover, a technique to represent continuum  $|e\bar{e}\rangle$  states improved over the discrete approach used here (for example, replacing them with an equivalent spectral function [16]) will produce numerically more stable results.

In addition to the analytical work required, including these additional Fock states will mandate a much larger numerical effort. While the new states could in principle just be added to the list of valence states included (just as  $|e\bar{e}\rangle$  and  $|e\bar{e}\gamma\rangle$  are this work), the numerical effort required to accommodate them is likely too great. For example, the sector  $|\mu\bar{\mu}e\bar{e}\rangle$  has 6 independent coordinates and 16 spin states. This sector alone would naively require  $16 \times N^6$  elements in each eigenvector, a number that is greater than the dimension of the entire Fock space considered in our toy model. Instead, the implementation of these Fock states will likely require developing an appropriate effective interaction for their successful incorporation into the calculation.

Once the component wave functions are computed by any suitable means, they are ready to incorporate directly into the calculation of any physical process. For example, the dissociative diffraction of pions in the pres-

ence of nuclear matter [39] (used to explore QCD color transparency [40]) employs distribution functions that, in the light-front form, are none other than the pion component wave functions [41]. Essentially the same physics, but applied to the much simpler QED case, appears in experiments discussed above [4] that probe the dissociation of true muonium on high- $Z$  targets.

## Appendix: Matrix Elements between Flavor Sectors

The relevant matrix elements for the calculation can be obtained through a straightforward generalization of the results in Ref. [14], particularly Appendix F. Those involving a single flavor ( $\mu$  or  $e$ ) are exactly the same as in Appendices F.1–F.3, once the appropriate fermion mass is used (not counting the subtraction in amplitude  $G_2$  of App. F.3 described in Sec. VI). We also correct a typo in the expression for amplitude  $G_3$  in [14]:  $1 - n \rightarrow 1 + n$ . Only the single-photon annihilation graphs (App. F.4) that mix the flavors differ. Denoting the initial and final fermion masses as  $m'$ ,  $m$ , respectively (and similarly for  $x$  and  $k_\perp$ ), the key kinematic quantity appearing in the propagators is the effective kinetic energy

$$\omega^* \equiv \frac{1}{2} \left[ \frac{m^2 + k_\perp^2}{x(1-x)} + \frac{m'^2 + k_\perp'^2}{x'(1-x')} \right], \quad (\text{A.1})$$

which is a slightly different  $\omega^*$  than is used for the standard annihilation graphs in the absence of  $e\bar{e}$ . This definition in either case has the special significance in the method of iterated resolvents, that it allows the truncation of neglected Fock states in a controlled manner. The amplitudes for the process then read:

$$I_1(x, k_\perp; x', k'_\perp) = \frac{\alpha}{\pi} \frac{2m'm}{\omega^*} \frac{1}{x(1-x)} \frac{1}{x'(1-x')} \delta_{|J_z|,1}, \quad (\text{A.2})$$

$$I_2(x, k_\perp; x', k'_\perp) = \frac{\alpha}{\pi} \left[ \frac{2}{\omega^*} \frac{k_\perp k'_\perp}{xx'} \delta_{|J_z|,1} + 4\delta_{J_z,0} \right], \quad (\text{A.3})$$

$$I_3(x, k_\perp; x', k'_\perp) = \frac{\alpha}{\pi} \frac{2m\lambda_1}{\omega^*} \frac{1}{x(1-x)} \frac{k'_\perp}{1-x'} \delta_{|J_z|,1}, \quad (\text{A.4})$$

$$I_4(x, k_\perp; x', k'_\perp) = -\frac{\alpha}{\pi} \left[ \frac{2}{\omega^*} \frac{k_\perp k'_\perp}{x'(1-x)} \delta_{|J_z|,1} - 4\delta_{J_z,0} \right]. \quad (\text{A.5})$$

Note that the only nonvanishing matrix elements have  $|J_z| \leq 1$ , a restriction due to the angular momentum of the photon. Abbreviating  $I_i(1,2) \equiv I_i(x, k_\perp; x', k'_\perp)$ , the amplitudes for all allowed combinations of helicity states are given in Table IV.

$m : m'$	$\uparrow\uparrow$	$\uparrow\downarrow$	$\downarrow\uparrow$	$\downarrow\downarrow$
$\uparrow\uparrow$	$I_1(1,2)$	$I_3(2,1)$	$I_3^*(2,1)$	0
$\uparrow\downarrow$	$I_3(1,2)$	$I_2^*(1,2)$	$I_4(2,1)$	0
$\downarrow\uparrow$	$I_3^*(1,2)$	$I_4(1,2)$	$I_2(1,2)$	0
$\downarrow\downarrow$	0	0	0	0

TABLE IV. Helicity table of the annihilation graph, where  $m$  and  $m'$  indicate the final-state and initial-state fermions, respectively.

## ACKNOWLEDGMENTS

We thank S. Brodsky for very useful conversations, and H.L. thanks U. Trittman for valuable insight into understanding his code. This work was supported by the National Science Foundation under Grant No. PHY-1068286.

- 
- [1] R. Coombes, R. Flexer, A. Hall, R. Kennelly, J. Kirkby, R. Piccioni, D. Porat and M. Schwartz *et al.*, Phys. Rev. Lett. **37**, 249 (1976).
  - [2] D.B. Cassidy and A.P. Mills, Nature (London) **449**, 195 (2007).
  - [3] S.J. Brodsky and R.F. Lebed, Phys. Rev. Lett. **102**, 213401 (2009) [arXiv:0904.2225 [hep-ph]].
  - [4] A. Banburski and P. Schuster, Phys. Rev. D **86**, 093007 (2012) [arXiv:1206.3961 [hep-ph]].
  - [5] A. Antognini, F. Nez, K. Schuhmann, F.D. Amaro, F. Biraben, J.M.R. Cardoso, D.S. Covita and A. Dax *et al.*, Science **339**, 417 (2013).
  - [6] D. Tucker-Smith and I. Yavin, Phys. Rev. D **83**, 101702 (2011) [arXiv:1011.4922 [hep-ph]].
  - [7] R.T. Robiscoe, Phys. Rev. **138**, A22 (1965).
  - [8] P.A.M. Dirac, Rev. Mod. Phys. **21**, 392 (1949).
  - [9] S.J. Brodsky, H.-C. Pauli and S.S. Pinsky, Phys. Rept. **301**, 299 (1998) [hep-ph/9705477].
  - [10] H.C. Pauli and S.J. Brodsky, Phys. Rev. D **32**, 2001 (1985).
  - [11] A.C. Tang, S.J. Brodsky and H.C. Pauli, Phys. Rev. D **44**, 1842 (1991).
  - [12] M. Krautgärtner, H.C. Pauli and F. Wölz, Phys. Rev. D **45**, 3755 (1992).
  - [13] M. Kaluža and H.C. Pauli, Phys. Rev. D **45**, 2968 (1992).
  - [14] U. Trittman and H.-C. Pauli, hep-th/9704215.
  - [15] S.J. Brodsky, R. Roskies and R. Suaya, Phys. Rev. D **8**, 4574 (1973).
  - [16] H. Lamm and R.F. Lebed, in preparation.
  - [17] G.P. Lepage and S.J. Brodsky, Phys. Rev. D **22**, 2157 (1980).
  - [18] I. Tamm, J. Phys. (USSR) **9**, 449 (1945).
  - [19] S.M. Dancoff, Phys. Rev. **78**, 382 (1950).
  - [20] H.-C. Pauli, hep-th/9608035.
  - [21] U. Trittman, in *Les Houches 1997, New non-perturbative methods and quantization on the light cone*, pp. 89-96 [hep-th/9706055].
  - [22] U. Trittman, hep-th/9705072.
  - [23] U. Trittman and H.-C. Pauli, Nucl. Phys. Proc. Suppl. **90**, 161 (2000).
  - [24] H.-C. Pauli, in *Nagoya 1996, Perspectives of strong coupling gauge theories*, pp. 342-352 [hep-th/9706036].
  - [25] U.D. Jentschura, G. Soff, V.G. Ivanov and S.G. Karshenboim, Phys. Rev. A **56**, 4483 (1997) [physics/9706026].
  - [26] B.D. Jones, R.J. Perry and S.D. Glazek, Phys. Rev. D **55**, 6561 (1997) [hep-th/9605231].
  - [27] B.D. Jones, hep-th/9703106.
  - [28] R. Karplus and A. Klein, Phys. Rev. **87**, 848 (1952).
  - [29] S.S. Chabysheva and J.R. Hiller, Phys. Rev. D **81**, 074030 (2010) [arXiv:0911.4455 [hep-ph]].
  - [30] S.S. Chabysheva and J.R. Hiller, Phys. Rev. D **82**, 034004 (2010) [arXiv:1006.1077 [hep-ph]].
  - [31] E.L. Gubankova, H.-C. Pauli and F.J. Wegner, hep-th/9809143.
  - [32] E.L. Gubankova and G. Papp, hep-th/9904081.

- [33] V.A. Karmanov, J.-F. Mathiot and A.V. Smirnov, Phys. Rev. D **77**, 085028 (2008) [arXiv:0801.4507 [hep-th]].
- [34] V.A. Karmanov, J.F. Mathiot and A.V. Smirnov, Phys. Rev. D **86**, 085006 (2012) [arXiv:1204.3257 [hep-th]].
- [35] P. Wiecki, Y. Li, X. Zhao, P. Maris and J.P. Vary, arXiv:1404.6234 [nucl-th].
- [36] C. Itzykson and J.-B. Zuber, *Quantum Field Theory*, McGraw-Hill, New York (1980).
- [37] D. Eiras and J. Soto, Phys. Lett. B **491**, 101 (2000) [hep-ph/0005066].
- [38] V.G. Ivanov, E.Y. Korzinin and S.G. Karshenboim, Phys. Rev. D **80**, 027702 (2009).
- [39] L. Frankfurt, G.A. Miller and M. Strikman, Phys. Lett. B **304**, 1 (1993) [hep-ph/9305228].
- [40] E.M. Aitala *et al.* [E791 Collaboration], Phys. Rev. Lett. **86**, 4773 (2001) [hep-ex/0010044].
- [41] D. Ashery, Prog. Part. Nucl. Phys. **56**, 279 (2006).